Supplement of Hydrol. Earth Syst. Sci., 24, 3229–3250, 2020
https://doi.org/10.5194/hess-24-3229-2020-supplement

Hydrology and Earth System Sciences
Open Access
EGU

Supplement of

Assessment of the geomorphic effectiveness of controlled floods in a braided river using a reduced-complexity numerical model

Luca Ziliani et al.

Correspondence to: Nicola Surian (nicola.surian@unipd.it)

Supplementary material

Contents of this file

Introduction

This supplementary material provides supplementary text concerning the CAESAR-LISFLOOD model (hereafter C-L) detailing several issues about the hydrodynamic and sediment transport numerical scheme, the lateral erosion and the vegetation component modules (Text S1). It also includes details concerning the C-L model calibration to the Piave River case study (Text S2) in addition to a specific focus on the sediment budget estimation carried out to enforce the calibration achievements (Text S3).

Text S1. Supplementary text on CAESAR-LISFLOOD model

C-L model general overview

In this study, CAESAR–LISFLOOD model [Coulthard et al., 2013] has been applied (version 1.2-modified, "reach mode" application – source code freely available at https://sourceforge.net/projects/caesar-lisflood/). This model is an integration of LISFLOOD-FP [Bates et al., 2010] and CAESAR [Coulthard et al., 2007; Van De Wiel et al., 2007] models.

C-L is a 2D hydro and morphodynamic model that discretizes the model domain into cells and calculate the flux of water and sediment across the two Cartesian boundaries of these cells (i.e. the X and Y directions) according to the quasi-linearized one-dimensional (1D) Saint Venant equation. C-L is founded on the cellular automaton (CA) concept, consisting in a continue local (i.e. grid scale) application of a set of relatively simple "rules", that are the drivers of the transport processes at the whole fluvial system scale. Although their linearity and simplicity, the effect of their iterated and combined application is such that also non-linear morphological response can be reproduced.

Flow routine

The C-L model embedded the LISFLOOD-FP model as internal flow routine scheme, in particular the so called LISFLOOD-ACC model (Neal et al., 2012), developed according to [Bates et al. 2010]. LISFLOOD-ACC is a two-dimensional inertial model, first order in space and explicit in time, that uses a semi-implicit treatment for the friction term to increase the numerical stability (Neal et al., 2012).

LISFLOOD-ACC assumptions emerge clearly starting from the quasi-linearized one-dimensional De Saint–Venant equation in its conservative form proposed in Eq. (1)

$$\frac{\partial Q_x}{\partial t} + \frac{\partial}{\partial x}\left[\frac{Q_x^2}{A_x}\right] + gA_x\frac{\partial h}{\partial x} + gA_x\,(S_{fx} - S_{0x}) = 0 \quad (1)$$

where Q_x [L^3T^{-1}] is the flowing discharge in the x direction, A_x [L^2] is the flow cross section area in the orthogonal direction y, g is the acceleration of gravity [LT^2], h is the water depth into the single cell [L], t is the generic time value [T], S_{fx} [] is the friction loss term and, S_{0x} [] the water slope friction term.

According to the Manning's law, the Equation **Errore. L'origine riferimento non è stata trovata.** can be rearranged to emphasize the main energy factors driving the momentum equilibrium condition of the control volume

$$\frac{\partial Q_x}{\partial t} + \frac{\partial}{\partial x}\left[\frac{Q_x^2}{A_x}\right] + \frac{gA_x\partial(h+z)}{\partial x} + \frac{gn^2Q_x^2}{R^{4/3}A_x} = 0 \quad (2)$$

where z is the bed elevation [L], R is the hydraulic radius [L], and n is the Manning's friction coefficient [$L^{-1/3}T$]. As demonstrated by Hunter et al. (2007), in contexts that are dominated bi-dimensional flow dynamic such as floodplains or wide shallow water braided rivers, the flows advection is relatively unimportant, so much to be essentially negligible [Bates et al., 2010]. In these situations, the area A_x can be assumed rectangular and the hydraulic radius R can be approximated to the flow depth h. Discretizing the equation with respect to the time, we obtain the following expression

$$\frac{Q_x[t+\Delta t]-Q_x[t]}{\Delta t} + \frac{g\Delta y h[t]\partial(h[t]+z)}{\partial x} + \frac{gn^2Q_x^2[t]}{\Delta y h[t]^{7/3}} = 0 \quad (3)$$

where Δy [L] is the cell dimension in the orthogonal flowing direction and Δt [T] is the model time step. Discretizing the equation also with respect to the space, we obtain

$$\frac{Q_{x;i,j}[t+\Delta t]-Q_{x;i,j}[t]}{\Delta t} + \frac{g\Delta y h_{i,j}[t](h_{i-1,j}[t]-h_{i,j}[t]+z_{i-1,j}-z_{i,j})}{\Delta x} + \frac{gn^2Q_{x;i,j}^2[t]}{\Delta y h_{i,j}[t]^{7/3}} = 0 \quad (4)$$

where Δx [L] is the cell dimension in the flowing direction, and (i, j) is the cell location in the grid. This equation can be explicitly solved in $Q_{x;i,j}[t+\Delta t]$, that is the unknown discharge in the generic (i, j) cell at the following $[t+\Delta t]$ simulation time step, as shown in Eq. (5).

$$Q_{x;i,j}[t+\Delta t] = Q_{x;i,j}[t] - g\Delta y\Delta t h_{i,j}[t]\left(\frac{h_{i-1,j}[t]-h_{i,j}[t]+z_{i-1,j}-z_{i,j}}{\Delta x} + \frac{n^2Q_{x;i,j}^2[t]}{\Delta y^2 h_{i,j}[t]^{10/3}}\right) \quad (5)$$

In Eq. (5) numerical instabilities may still arise at shallow depths when the friction term becomes large. To overcome this issue, Bates et al. (2010) proposed to replace the $Q_{x;i,j}[t]$ in the friction term by $Q_{x;i,j}[t+\Delta t]$ leading to an equation linear in the unknown $Q_{x;i,j}[t+\Delta t]$ which has some of the improved convergence properties of an implicit time stepping scheme (so

the expression “semi-implicit treatment for the friction term” used by Neal et al. (2011)). Following the substitution, we achieve

$$Q_{x;i,j}[t+\Delta t] = Q_{x;i,j}[t] - g\Delta y\Delta t h_{i,j}[t]\left[\frac{h_{i-1,j}[t]-h_{i,j}[t]+z_{i-1,j}-z_{i,j}}{\Delta x} + \frac{n^2 Q_{x;i,j}[t+\Delta t]Q_{x;i,j}[t]}{\Delta y^2 h_{i,j}[t]^{10/3}}\right] \quad (6)$$

that can be rearranged in the $Q_{x;i,j}[t+\Delta t]$ explicit form

$$Q_{x;i,j}[t+\Delta t] = \frac{Q_{x;i,j}[t]-g\Delta y\Delta t h_{i,j}[t]\left(\frac{h_{i-1,j}[t]-h_{i,j}[t]+z_{i-1,j}-z_{i,j}}{\Delta x}\right)}{1+\left(\frac{g\Delta t h_{i,j}[t] n^2 Q_{x;i,j}[t]}{\Delta y h_{i,j}[t]^{10/3}}\right)} \quad (7)$$

The stability of Eq. (7) in shallow depth conditions is guaranteed because the denominator increases as the friction term increases, forcing the flow to zero, as would be expected.

Having established the discharge across all four boundaries of a cell (D4 scheme is adopted), the cell water depth is updated using the mass conservation equation in the following form:

$$h_{i,j}[t+\Delta t] = h_{i,j}[t] + \Delta t\frac{Q_{x;i-1,j}[t+\Delta t]-Q_{x;i,j}[t+\Delta t]+Q_{y;i,j-1}[t+\Delta t]+Q_{y;i,j}[t+\Delta t]}{\Delta x\Delta y} \quad (8)$$

where *i* and *j* are cell co-ordinates. For each grid cell the mass balance is updated at each time step according to the fluxes of water across the four boundaries of each cell.

Equations (7) and (8) represent the core of the flow routine because they allow the direct solution of the mass and momentum equilibrium problem. Assuming that bed elevation $z_{i,j}[t_0]$, water stage $h_{i,j}[t_0]$ and discharge $Q_{y,x;i,j}[t_0]$ are known at the initial time step t_0 in each (i,j) cell of the domain (as per the initial and boundary conditions), at the following generic $t_0+\Delta t$ time step $Q_{x,y;i,j}[t_0+\Delta t]$ and $h_{i,j}[t+\Delta t]$ can be explicitly calculated.

Equation (7) includes shallow water wave propagation so it is still subject to the Courant–Freidrichs–Levy (CFL) condition that is

$$C_r = \frac{V\Delta t}{\Delta x} < 1 \quad (9)$$

where C_r is the non-dimensional Courant number, V is the characteristic velocity [LT^{-1}], that in shallow water condition (negligible advection term) is equal to the celerity of a long wavelength, small amplitude gravity wave ($\sqrt{gh}$). The CFL condition itself is not sufficient to ensure model stability, because the assumption of small amplitude in calculating the wave celerity is not always valid, and because of the inclusion of friction terms in the model. So, the Courant number value can be defined by the user (see Table 3 in the main text) in the range 0.2 – 0.7, introducing a further constrain (α value) to the maximum time step as in the following equation

$$\Delta t_{max} = \alpha\frac{\Delta x}{\sqrt{gh}} \quad (10)$$

Sediment transport – Bed and suspended load

Water depth and velocity fields calculated by the flow routine described in the previous section are then used to calculate the shear stress, in turn used to estimate the bedload transport (two available formulae, Einstein (1950) and Wilcock and Crowe (2003) – see Table 3 in the main text). C-L model allows routing as bedload up to nine grainsize classes (whose characteristic diameters are defined by the modeler), while only one grain size (the finest) can be transported as suspended. The adoption of a multi-grain system, and the following selective processes of erosion/transport/deposition/armouring, allows to model a sediment size distribution that is spatially variable, not just horizontally but also vertically. In particular the vertical variability is carried out through the adoption of an active layer scheme similar to that proposed in Parker (1990), Hoey and Fergusson (1994) and Toro-Escobar et al. (1996). From the top to the bottom of the whole alluvial package, the scheme consists of a superficial layer (i.e. the active layer), multiple buried strata, a base layer and a fixed not erodible bedrock layer.

The active layer has a variable thickness in the range [0.25÷1.5] L_h, where L_h is a parameter defined by the modeler (see Table 3 in the main text). The buried strata have a fixes thickness equal to L_h, and they are present in a number of 10 (value not editable through the graphical interface). In case of erosion, the active layer thickness decreases up to the minimum value of $0.25L_h$. When the minimum is reached, the upper buried strata is merged to the active layer forming a new active layer, whereas a new buried strata is created if enough material is available in the base layer. If erosion continues and the bedrock is reached, the erosion is stopped. In case of deposition, if the active layer thickness reached the $1.5L_h$ value, a new strata is created leaving a thinner active layer and a new buried layer is formed. If the deposition proceeds and 20 buried strata are present, the lowest buried layer is included into the base layer. For further details see [Coulthard et al., 2002] and [Van De Wiel et al., 2007].

To avoid numerical instabilities and "checker boxing" of the erosion pattern due to excessive vertical erosion, a maximum erosion value has to be fixed by the modeler (i.e. 'Maximum erosion limit' in Table 3 in the main text). The computation time step is dynamically reduced up to the maximum erosion for each time step (i.e. per iteration) is respected over all the domain.

The bedload formula provides the sediment flux is moving from each wet cell. The distribution of the transported sediment is then defined through the following simple in-channel lateral erosion function:

$$\Delta z_{i-1,j} = \Delta z_{i,j} L \frac{(z_{i-1,j} - z_{ij})}{\Delta x} \quad (11)$$

where the amount of sediment transferred from the donner (*i, j*) cell ($\Delta z_{i-1,j}$) to the adjacent cell (*i-1, j*) included in the D4 scheme, is proportional to the amount eroded from the donner ($\Delta z_{i,j}$), a constant *L* (the 'in-channel lateral erosion rate' - see Table 3 in the main text) and the slope between cells, $\frac{(z_{i-1,j} - z_{ij})}{\Delta x}$ (as far as both cells have a water depth equal or greater than the model parameter 'water depth above which erosion can happen', a user-defined parameters reported in Table 3 in the main text). The *L* parameter ('In-channel lateral erosion rate' in Table 3 in the main text) controls the narrowing/widening of

the flowing part of the channel; it represents how much cohesive or incoherent the sediment is: if sediment is loosely packed and unconsolidated, then it is readily eroded, laterally transported (within the channel) and results in a shallow wide channel. If it is more cohesive, harder to move laterally, then a narrower deeper channel results. For further details see [Coulthard et al., 2013].

The entrainment (i.e. resuspension) of the finest grain class is driven by the bedload sediment transport formula. If suspended sediment is present into the water column above a cell it moves to the D4 neighbourhood cells with the same water velocity. The suspended sediment flux (in m^3s^{-1}) is calculated according to the following Eq. (12)

$$Q_s = Q\ {}^{S_{tot}}/_{h} \tag{12}$$

where Q is the flowing discharge in m^3s^{-1}, S_{tot} is the total amount of suspended sediment [m] and h the water depth in the cell. Then as per the conservative mass equation the mass of sediment is corrected as follow

$$\frac{\Delta S_{tot}}{\Delta t} = \frac{Qs_x^{i-1,j} - Qs_x^{i,j} + Qs_y^{i,j-1} - Qs_y^{i,j-1}}{\Delta x^2} \tag{13}$$

Suspended sediment is then deposited according to the settling velocity as defined by the modeler.

Lateral erosion model

Lateral erosion process is reproduced through several dedicated routines organized in three main phases: (i) calculation of the local channel curvature, (ii) calculation of the lateral eroded volume and (iii) eroded sediment distribution. The curvature calculation is achieved following several steps: the first identifies the edge cells searching for those dry cells with at least one wet neighbour in one of the four primary (i.e. non-diagonal) directions cell. 'Wet' are those cells where the water depth is greater than the 'water depth above which erosion can happen', one of the user-defined parameters (see Table 3 in the main text). Secondly a simple procedure is applied to discern edge cells that are coincident to inside or outside bend: the sign of the local radius of curvature (R_c) defines this attribution ($R_c > 0$ – outside; $R_c < 0$ – inside). The R_c is calculated roughly passing of a 9-cells filter over the grid: where the filter is centred in an edge cell, both the number of dry and wet cells are counted, excluding other edge cells in the same window (only the largest connected series of wet cells in the filter is considered to avoid inside banks false positive in case of near cut-off). The local rough R_c local value is then estimated and assigned to the edge cell subtracting the number of wet cells from dry. The R_c value so achieved is then smoothed through the application of a further averaging filter that is passed over the edge cells (the 'number of passes for edge smoothing filter' is another user-defined parameter – see Table 3 in the main text). Finally, a cross-stream gradient of the R_c value is determined by the application of an averaging windows moved across the wet cells to linearly interpolate the R_c values between channel edges. The final R_{ca} value is dimensionless approximation of the actual radius of curvature. After radius of curvature have been calculated for each edge cells, the lateral erosion rates, ζ, are calculated from a relation inspired by other vector-based linearized meanders models (Ikeda et al., 1981; Blondeaux and Seminara, 1985):

$$\zeta = \Delta z_{i-1,j} = -\Delta z_{i,j} E R_{c,i-1}\ \frac{(z_{i-1,j} - z_{ij})}{\Delta x} \tag{14}$$

where (*i, j*) is a dry donner edge cell, (*i-1,* j) is an adjacent wet receiver cell, E is the 'lateral erosion rate' dimensionless coefficient (see Table 3 in the main text), U_{nb} and h_{nb} respectively denote the flow velocity and water depth in the wet cells neighbouring the edge cell (i.e. wet near-bank cells). ζ represents the volume eroded by the lateral erosion process in the bank cells (dimensionally it is [L]). It is expressed as thickness of sediment removed from each cell at the single computational time step. The laterally eroded volume is moved from the edge cell towards the inner part of the channel bend in the D4 neighbour cells only.

It is important to stress that there is no physical basis for assuming that the technique adopted in the model, based on the cross-stream gradient of curvature, would actually govern lateral sediment distribution. This is only a simplification of a process mainly driven by secondary flow. Since, in this cellular model there is no representation of secondary circulation, sediment is transported according to local downward slopes. For more details about the lateral erosion module see [Coulthard and Van De Wiel, 2006], [Van De Wiel et al.; 2007] and [Coulthard et al., 2013].

The lateral erosion scheme as described above was adopted originally in C-L since 1.1d version and rebuilt in the 1.2 version modified here adopted.

Vegetation component

The vegetation module adopted in C-L arises from a slight refinement of the corresponding module adopted in CAESAR [Coulthard et al., 2007]. 'Vegetation' is not a specific plant, bush, grass or tree, but is concerned with how vegetation in general will impact on fluvial processes. The presence of the vegetation and its effect on the sediment dynamic are function mainly of its 'maturity', a lumped parameter used as a proxy of aging, density and resistance to uprooting. The vegetation maturity (a dimensionless variable) ranges between 0 and 1 growing over time. Wherever the water depth is under the user-defined value 'water depth above which erosion can happen', the vegetation growth rate is constant and inferred from the 'Vegetation maturity' parameter (see Table 3 in the main text) that is the number of years required to have a fully vegetation growth from 0 to 1. The vegetation maturity increases for each model iterations until the maximum level (i.e. a maturity of 1) is reached. Whilst a vegetated cell is submerged, vegetation dies with a rate two times faster than growth. If bed shear stress exceeds a defined threshold value ('Vegetation critic shear' in Table 3 in the main text), vegetation is scoured away, and growth reset to zero. Moreover, vegetation can grow through sediments if buried, but if the burying layer is too thick, vegetation will die back and eventually regrow on surface. There are no additional feedbacks with vegetation, i.e., affecting evaporation rates or roughness parameters. No colonization or seed dispersal mechanisms are modeled.

The vegetation component provides effects exclusively acting to prevent or restrict erosion happening. The restriction is defined proportionally to the so called 'Proportion of erosion that can occur when vegetation is fully grown'. This parameter determines how vegetation maturity affects both the in-channel and lateral erosion rate. If set to 0 then, elsewhere the vegetation is fully grown (i.e. a maturity of 1) there can be no erosion whether using in-channel or lateral erosion. If set to 1, then vegetation will have no effect on sediment dynamic and erosion will occur whatever. If set to 0.1 (fixed value here adopted as this parameter has not been included in the calibration procedure), this means that when vegetation is fully grown

(a maturity of 1) then 10% of normal in-channel and lateral erosions will be allowed. This changes according to the maturity, so then the amount of erosion allowed will vary from 0.1 (with maturity of 1) to 1 (with a maturity of 0).

Assessment of factor sensitivity

Approaching this study, we've assumed the results presented in [Ziliani et al., 2013] as the main reference for the parameters sensitivity. In [Ziliani et al., 2013] the authors applied a two-step sensitivity analysis to CAESAR model, the geomorphic component of C-L herein used. The identification of the key parameters achieved by the sensitivity analysis allowed the authors to address more effectively the calibration step, tuning only the two most important quantitative parameters among those initially investigated (12). Analogously, in this work we've calibrated the C-L model tuning particularly the parameter identified as the much more sensitive in [Ziliani et al., 2013], that are the 'max erode limit' and the 'lateral erosion rate' (see Table 3 in the main text). A fully comprehensive model evaluation strategy of C-L model, adopting the same sound strategy presented in [Ziliani et al., 2013], would have required a significant computing effort that would be beyond the main goals of this work. We are aware that the results achieved for CAESAR model only are not perfectly applicable to C-L model, but we consider reasonable the assimilation here implicitly adopted.

Text S2. Supplementary text on model calibration

Performance indices

The performance indices here adopted (vegetation performance index - F_{veg}, wet area performance index - F_{wet}, active channel performance index - F_c) reference at all to a performance technique defined by Aronica et al. [2002], using indices developed specifically for raster dataset by Bates and De Roo [2000] and Horritt and Bates [2001]. The indices have been here used during the calibration procedure to quantify the capability of C-L model to spatially reproduce several hydro-morphological features (i.e., active channel widening / narrowing, wet area dynamic, vegetation cover evolution). They determine a pixel-to-pixel correspondence between a spatially distributed model output variable (i.e. wet area, vegetated area) and a raster data (real data derived through aerial photos digitalization and rasterization) with the same spatial resolution. All the performance indices used could be generically expressed in the form

$$F = \frac{S_{model} \cap S_{real}}{S_{model} \cup S_{real}} = \frac{\sum_{i=1}^{n} P_i^{R_1 M_1}}{\sum_{i=1}^{n} P_i^{R_1 M_1} + \sum_{i=1}^{n} P_i^{R_1 M_0} + \sum_{i=1}^{n} P_i^{R_0 M_1}} \quad (15)$$

where S_{model} and S_{real} are respectively the areas predicted by the model and the real area, n is the number of pixels in which that areas are rasterized, $P_i^{R_0 M_1}$ and $P_i^{R_1 M_0}$ are respectively a pixel where the variable is predicted by the model (M_1) but absent in the real data (R_0) and a pixel where the same quantity is absent in output model raster (M_0) but present in the field data (R_1), and $P_i^{R_1 M_1}$ and $P_i^{R_0 M_0}$ are pixels where model has correctly predicted the presence (R_1M_1) or absence (R_0M_0) of the same investigated variable. A detailed description of these components is reported in Table S1.

Initial and boundary conditions

The initial and boundary conditions used in the calibration step are listed and briefly described Table S2.

Results

The calibration runs covered the July 5th 2003 – August 5th 2009 period (2,223 days). During this time the flow regime has been characterized by several flood events (nine events with over one year Recurrence Interval, maximum peak 478 m^3s^{-1}) able to induce not negligible morphological changes. The flow regime observed during the calibration period can be considered representative of the average annual flow regime. As reported in Table S3 and shown in Figure S1 (i) the river reach has underwent a slight narrowing of the active channel (ca 13%, the active channel width decreased from 277 meters in 2003 to 241 meters in 2009) coupled to a negligible widening (2,5%) of the total channel width (i.e. the active channel width summed to the islands); (ii) the percentage of the total channel area occupied by vegetation (low-medium-high vegetation in islands and high bars, see Surian et al. 2014) has been doubled increasing from the ca 13% in 2003 up to ca 25% in 2009; (iii) the braiding index decreased (not significantly as per its dependence to the flowing discharge at the aerial photos acquirement moment). These evidences show that the 20% of the total channel experienced a morphological dynamic strictly related to the sediment transport and vegetation dynamics during the 2003-2009 period. In particular, nearly 5% of the channel area has been characterized by net lateral erosion process and 15% by vegetation establishment. Although the calibration referred to a period not featured by particularly large high flow events, both conditions of channel stability and morphological dynamic has been observed and used for the assessment of the model reliability reproducing both these situations of low and high dynamic. The presence of extreme floods in the calibration period would have likely increased the model reliability at all but even so would not have guaranteed the ability to reproduce the effect of events of comparable magnitude over long term scenarios.

Overall n. 76 runs have been performed during the calibration phase (total computational time ca 135 days) adopting a trial-and-error strategy (i.e. manual calibration). According to the results achieved through the sensitivity analysis carried out by Ziliani et. al (2013) the 'lateral erosion rate' and 'maximum erode limit' factors (see Table 3 in the main text) were primary tuned. For each simulation all the performance index previously detailed has been calculated, in addition to other main morphometric values such as the active channel width, the wet channel width and the braiding index (see box plot of the results in Figure S2). The final best calibration setting has been identified referring mainly to the active channel width value and the braiding index trying to obtain a difference between the modeled and the real values lower than respectively the domain cell size (10 m) for the width and the 2% for the BI. The mean water depth has not been used as a calibration reference value because of the lack of data concerning the river bathymetry.

The assessment of the calibration final run results in terms of (i) morphological pattern (see Figure 5 in the main text, Figure S3 and S4 in the supplementary information files), (ii) morphological overall performance (Table 4 in the main text) and (iii)

difference between the real and the modeled active channel width and braiding index (Table 4 in the main text), induce the authors to consider the calibration achievement as widely acceptable.

Text S3. Supplementary text on sediment yield estimation

The annual sediment yield estimation has been performed to enforce the confidence on the model reliability at the end of the calibration step. By doing so, the assessment of the model performance in terms of morphological answer has been coupled to the assessment of its capability in reproducing the annual sediment fluxes as well.

The sediment yield has been calculated every year in the 2003-2009 period (i.e. 6 years in total) analysing output net solid fluxes along the reach during the calibration run (the final calibration setting has been adopted). The fluxes have been measured at the downstream end of each sub-reach (ca 1 km length) we have divided the Piave River reach (see Figure S3). During the simulation the model factor 'Sediment Proportion Recirculated' (see Table 3 in the main text) has been fixed equal to be 1, which implies assuming the upstream sediment loading the same as at the output end of the whole reach.

The modeled average bed load sediment yield resulted of about 21.5 x 10^3 m^3yr^{-1}. As shown in Figure S3, modeled yield varies significantly along the reach (up to 30%) ranging between 14.8 ÷ 29 x 10^3 m^3yr^{-1}, with higher yearly values in the sub-reach just upstream San Pietro in Campo. The 2006 minimum corresponds to an average annual sediment yield of about 260 m^3yr^{-1} versus the 2008 maximum of about 53.3 x 10^3 m^3yr^{-1}.

The modeled mean annual sediment yield has the same order of magnitude of other estimates available in literature for gravel-bed rivers with similar characteristics to the Piave River reach under investigation (Vedder R.: 36.6 ± 5.6 x $10^3m^3yr^{-1}$ [Martin and Church, 1995]; Chilliwack R.: 4.9 ÷ 55 x $10^3m^3yr^{-1}$ [Ham and Church, 2000]; Waimakariri R. reach km 10.1-13.3: 60 x $10^3m^3yr^{-1}$ [Nicholas, 2000]; Eygues R.: 66 x $10^3m^3yr^{-1}$ [Liebault et al., 2008]; Brenta R.: 70 x $10^3m^3yr^{-1}$ [Surian and Cisotto]).

The comparison with literature values has been carried out due to lack of site-specific data that would have allowed to achieve even only gross local estimations (i.e. bedload transport measurements, continued detailed topographic sections or LiDAR surveys).

References

Aronica, G., P. D. Bates, and M. S. Horritt (2002), Assessing the uncertainty in distributed model predictions using observed binary pattern information within GLUE, Hydrol. Processes, 16(10), 2001-2016, doi:10.1002/hyp.398.

Bates, P. D. and A. P. J. De Roo (2000), A simple raster-based model for flood inundation simulation, J. Hydrol., 236(1-2), 54-77, doi:10.1016/S0022-1694(00)00278-X.

Bertoldi, W., A. Gurnell, and N. A. Drake (2011), The topographic signature of vegetation development along a braided river: Results of a combined analysis of airborne LiDAR, color air photographs, and ground measurements, Water Resour. Res., 47, W06525.

Blondeaux P., Seminara G., 1985. A unified bar-bend theory of river meanders. Journal of Fluid Mechanics 157, 449–470.

Coulthard, T. J., M. G. Macklin, and M. J. Kirkby (2002), A cellular model of Holocene upland river basin and alluvial fan evolution, Earth Surf. Processes Landforms, 27(3), 269-288, doi:10.1002/esp.318.

Coulthard, T.J., Van De Wiel, M.J., 2006. A cellular model of river meandering. Earth Surface Processes and Landforms 31, 123–132.

Coulthard, T. J., D. M. Hicks, and M. J. Van De Wiel (2007), Cellular modelling of river catchments and reaches: Advantages, limitations and prospects, Geomorphology, 90(3-4), 192-207, doi:10.1016/j.geomorph.2006.10.030.

Coulthard, T. J., J. C. Neal, P. D. Bates, J. Ramirez, G. A. M. de Almeida, and G. R. Hancock (2013), Integrating the LISFLOOD-FP 2D hydrodynamic model with the CAESAR model: Implications for modelling landscape evolution, Earth Surf. Process. Landforms, 38(15), 1897-1906.

Einstein, H. A. (1950), The bed-load function for sediment transport on open channel flows, in Tech. Bull., vol. 1026, USDA, Soil Conservation Service.

Ham, D. G. and M. Church (2000), Bed-material transport estimated from channel morphodynamics: Chilliwack River, British Columbia, Earth Surf. Processes Landforms, 25(10), 1123-1142.

Hoey T., Fergusson R. (1994), Numerical simulation of downstream fining by selective transport in gravel bed rivers: Model development and illustration. Water Resources Research 30(7): 2251–2260.

Horritt, M. S. and P. D. Bates (2001), Predicting floodplain inundation: Raster-based modelling versus the finite-element approach, Hydrol. Processes, 15(5), 825-842, doi:10.1002/hyp.188.

Ikeda S., Parker G., Sawai K., 1981. Bend theory of river meanders: I. Linear development. Journal of Fluid Mechanics 112, 363–377.

Liebault, F., H. Piegay, P. Frey, and N. Landon (2008), Tributaries and the management of main-stem geomorphology, in River Confluences, Tributaries and the Fluvial Network, edited by S. P. Rice, A. Roy and B. L. Rhoads, Wiley.

Martin, Y. and M. Church (1995), Bed-material transport estimated from channel surveys: Vedder River, British Columbia, Earth Surface Processes & Landforms, 20(4), 347-361.

Nicholas, A. P. (2000), Modelling bedload yield braided gravel bed rivers, Geomorphology, 36(1-2), 89-106, doi:10.1016/S0169-555X(00)00050-7.

Parker (1990), Surface-based bedload transport relation for gravel rivers, Journal of Hydraulic Research, 28, 417-436.

Surian, N. and A. Cisotto (2007), Channel adjustments, bedload transport and sediment sources in a gravel-bed river, Brenta River, Italy, Earth Surf. Processes Landforms, 32(11), 1641-1656, doi:10.1002/esp.1591.

Surian N, Barban M, Ziliani L, Monegato G, Bertoldi W, Comiti F (2014) Vegetation turnover in a braided river: frequency and effectiveness of floods of different magnitude. Earth Surf Proc Land 40:542–558. doi:10.1002/esp.3660

Toro-Escobar CM, Parker G, Paola C. 1996. Transfer function for the deposition of poorly sorted gravel in response to streambed aggradation. Journal of Hydraulic Research 34: 35–51.

Van De Wiel, M. J., T. J. Coulthard, M. G. Macklin, and J. Lewin (2007), Embedding reach-scale fluvial dynamics within the CAESAR cellular automaton landscape evolution model, Geomorphology, 90(3-4), 283-301, doi:10.1016/j.geomorph.2006.10.024.

Wilcock, P. R. and J. C. Crowe (2003), Surface-based transport model for mixed-size sediment, Journal of Hydraulic Engineering, 129(2), 120-128.

Figure S1 – (a) 2003 aerial photos (photos provided by: Autorità di Bacino delle Alpi Orientali), (b) 2003 digitized main morphological features, (c) 2009 aerial photos, (d) 2009 digitized main morphological features, (e) morphological features changes in 2003-2009, (f) morphological processes in 2003-2009

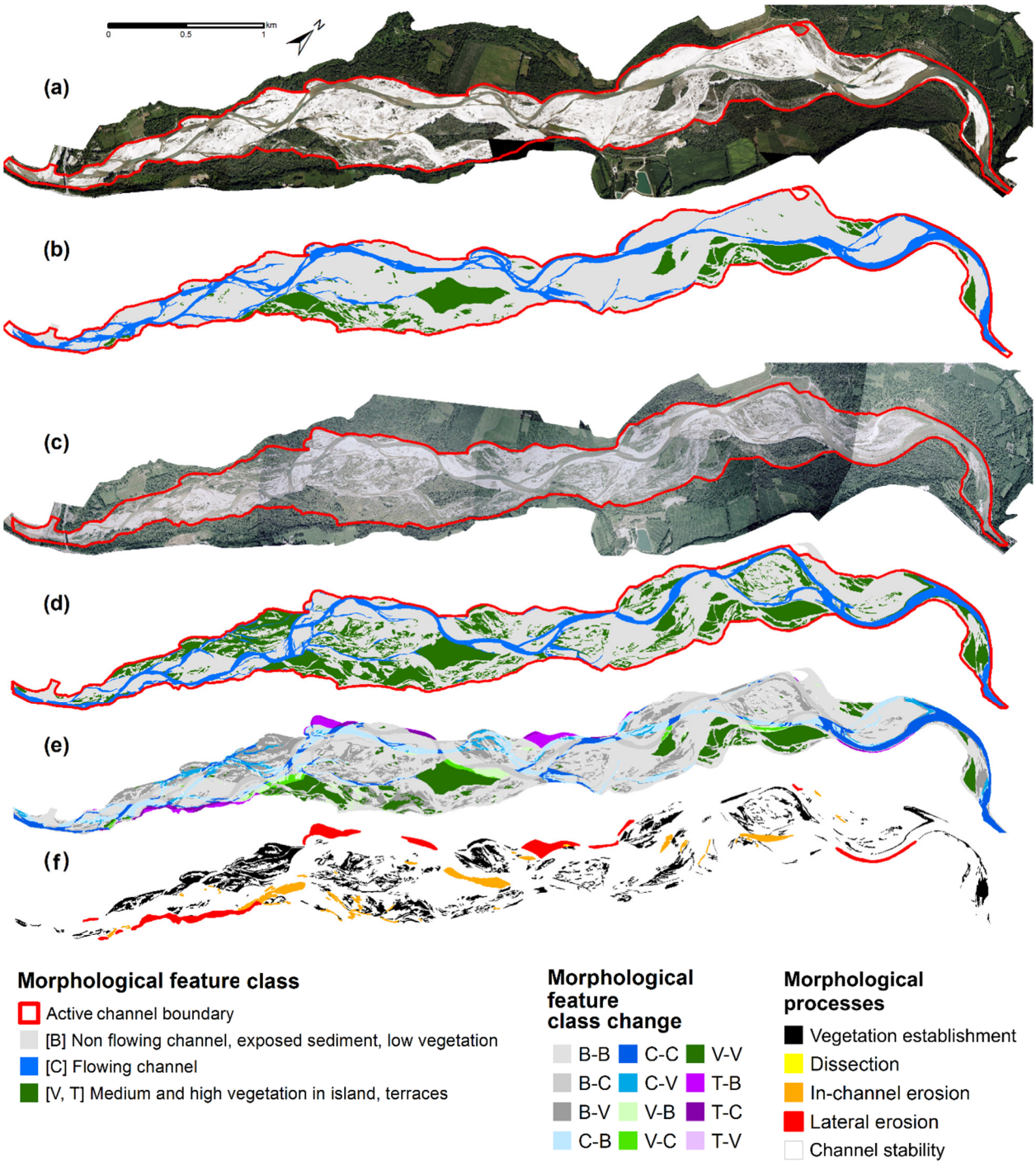

Figure S2 – Box plots of the main results achieved during calibration runs. (a) active channel width, (b) wet channel width, (c) braiding index value, (d) active channel performance index - F_c, (e) vegetation performance index - F_{veg}, (f) wet area performance index - F_{wet}

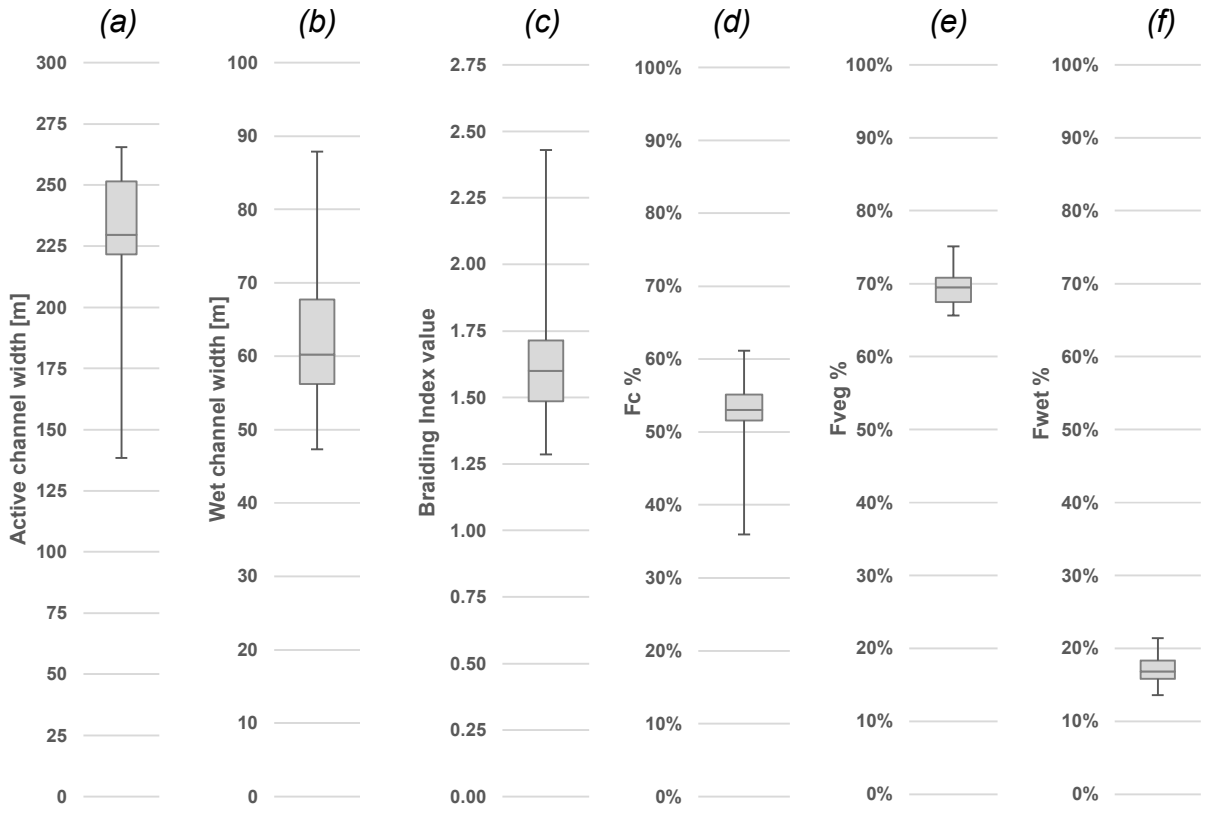

315

Figure S3. Model performance assessment at the end of the calibration runs (upstream frame): (a) wet area (b) vegetated area and (c) active channel digitalized using 5th August 2009 aerial photos; (d) overlay between modeled and observed flowing channel; (e) overlay between modeled and vegetated area; (f) overlay between modeled and observed active channel; (g) wet area performance index calculation; (h) vegetated area performance index calculation; (i) active channel performance index calculation

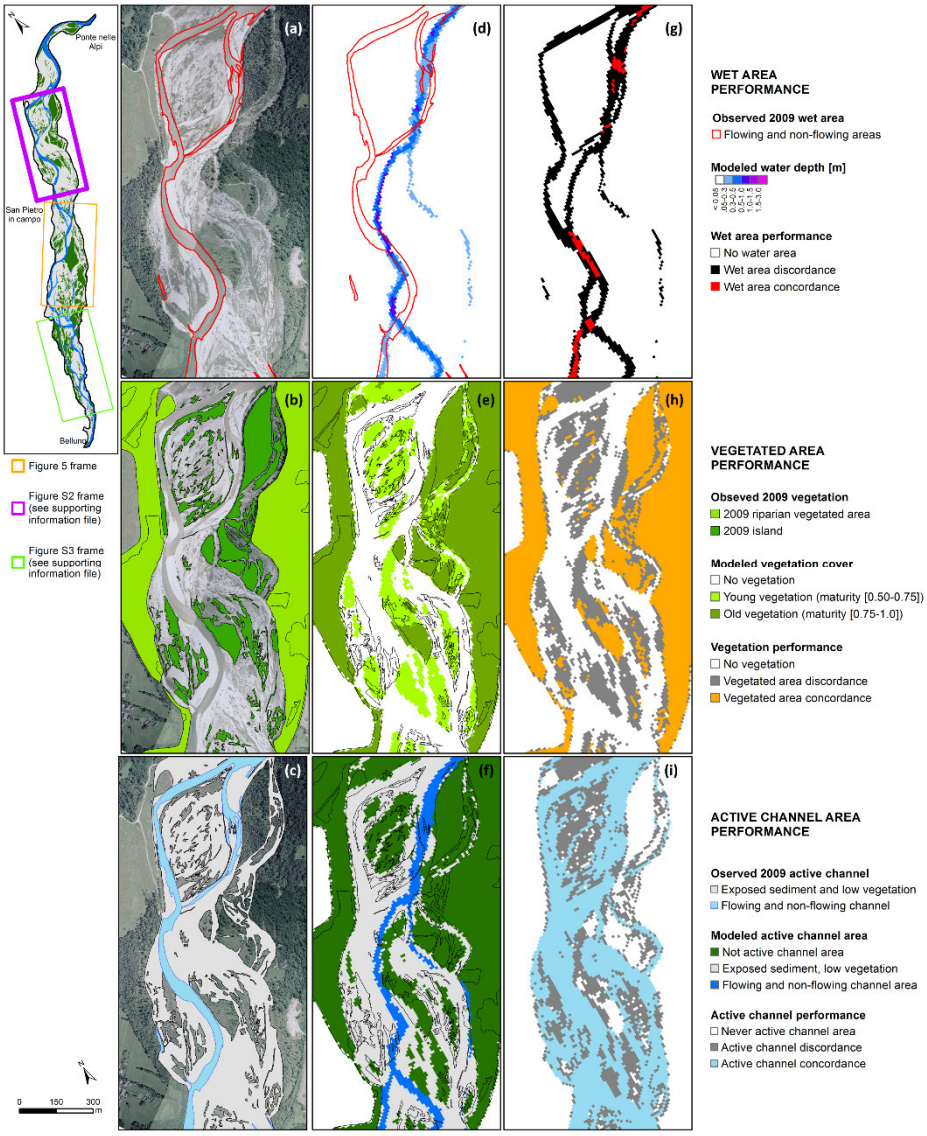

Figure S4. Model performance assessment at the end of the calibration runs (downstream frame): (a) wet area (b) vegetated area and (c) active channel digitalized using 5th August 2009 aerial photos; (d) overlay between modeled and observed flowing channel; (e) overlay between modeled and vegetated area; (f) overlay between modeled and observed active channel; (g) wet area performance index calculation; (h) vegetated area performance index calculation; (i) active channel performance index calculation

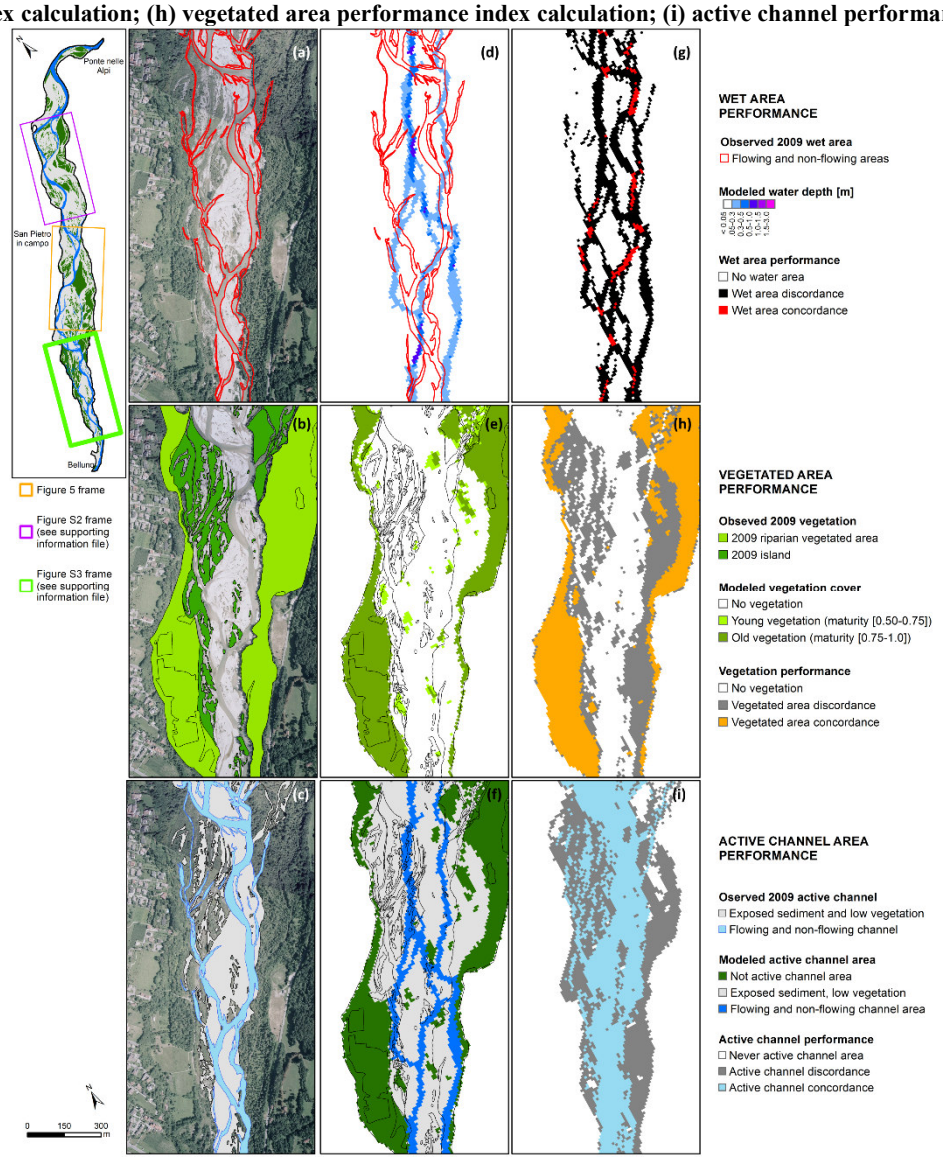

325

Figure S5 – Mean, maximum and minimum modeled annual bedload yield modeled for the 2003–2009 period along the whole study reach

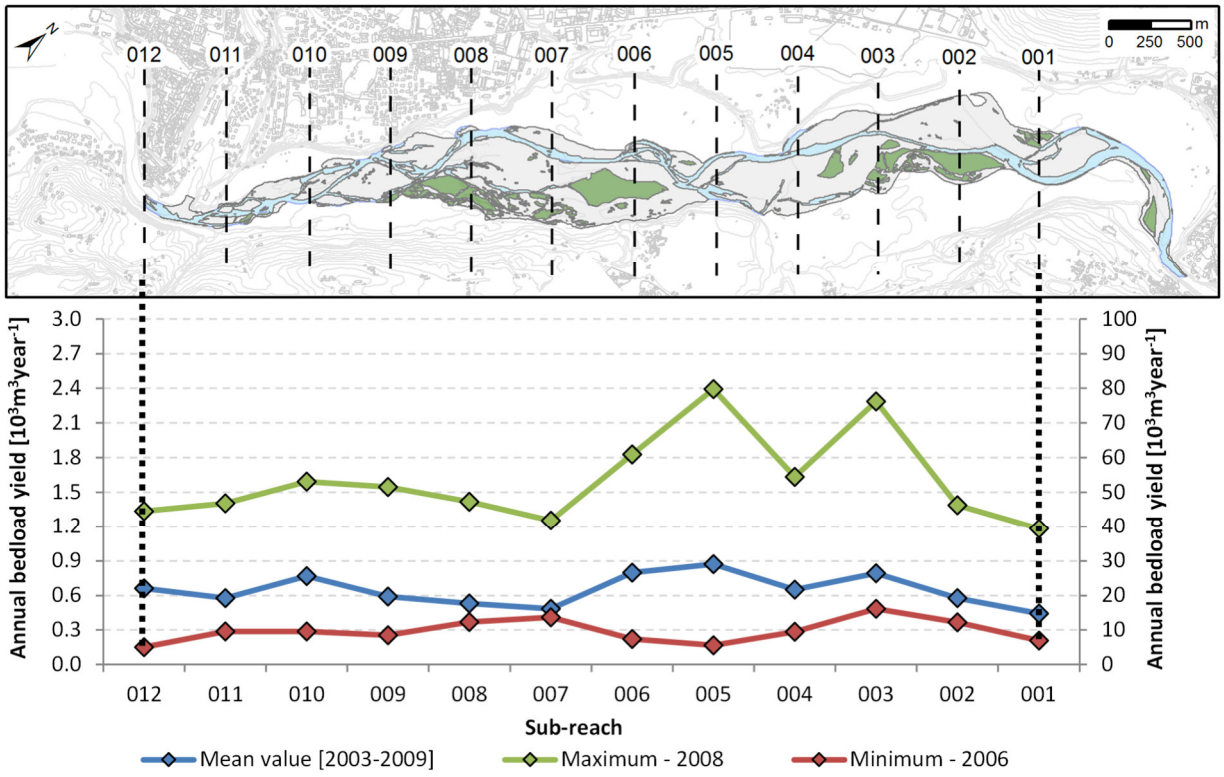

Table S1. Performance index description

Index	Assessed variable	M_1 cells – variable predicted by the model at the end of the simulation (August 5th 2009)	M_0 cells – variable not predicted by the model at the end of the simulation (August 5th 2009)	R_1 cells – variable observed in aerial photos acquired at August 5th 2009	R_0 cells – variable absent in aerial photos acquired at August 5th 2009
F_{veg}	Vegetation	*veg* > 0.5	*veg* <= 0.5	*GU* medium and high vegetation *	*GU* flowing channels, non-flowing channels, exposed sediments, low vegetation *
F_{wet}	Wetted area	*h* > 5 cm	*h* <= 5 cm	*GU* flowing channels *	Other *GUs* *
F_c	Active channel	(*h* > 5 cm) OR ((*h* <= 5 cm) AND (*veg* <= 0.5))	(*h* <= 5 cm) AND (*veg* > 0.5)	*GU* flowing channels, non-flowing channels, exposed sediments *	Other *GUs* *

veg = vegetation maturity; *h* = water depth; *GU* = geomorphological units

* as defined in [Surian et al., 2014]

330

Table S2. Initial and boundary conditions

Class	I / B *	Description
Hydraulic	I	The initial bed elevation was established using a 10 m cell DEM achieved resampling the available 2003 LiDAR DEM (bilinear interpolation, original cell dimension 2×2 m). The DEM was corrected in the wetted areas (about 8% of the total spatial domain) through the application of the method proposed in Bertoldi et al. [2011]
	B	Hourly discharge series (see Figure 2 in the main text) measured at Belluno gauge station (located at the downstream end of the reach)
	B	The wetted cell located at the downstream end of the model domain have a fixed steady flow hydraulic condition. The energy slope is defined by the modeler setting the parameter so called 'slope for edge cells'
Sedimentological	I	The initial texture of the bed surface and sub-surface, overall the erodible domain has been so defined: C1-[6.8mm], 27.4%; C2-[9.7mm], 5.2%; C3-[13.7mm], 6.2%; C4-[19.3mm], 7.2%; C5-[27.3mm], 9.2%; C6-[38.6mm], 10.2%; C7-[54.6mm], 10.2%; C8-[77.3mm], 12.2%; C9-[109.25mm], 14.3%. The percentage for each class (9 in total, C1-C9), has been set according to the most recent available grain size measurements (n. 6 samples, volumetric method) as reported in Tomasi [2009]. The bedrock elevation has been set everywhere 15 m below the initial bed surface. In the 'not erodible areas' (i.e. channelization structures, Holocene fluvial terraces boundaries) the bedrock has been set at the same elevation of the bed surface
Vegetation	I	The initial vegetation cover was carried out referring to the vegetation features digitalized using the 2003 aerial photos. Only the geomorphological features "medium and high vegetation" (as defined in Surian et al. 2014) were used. The vegetation maturity in the vegetated area was set to 1 and 0 elsewhere.

[*] *I*= initial condition; *B*= boundary condition

Table S3. 2003-2009 observed main morphological features and adjustments

	2003	2009	2003-2009 variation
Average active channel width [m]	277	241	- 12,9%
Total channel(*) width [m]	318	326	+ 2,5%
Average wet channel width [m]	57	51	- 10 %
Percentage of the total channel occupied by islands	12,9%	24,8%	+ 11,9%
Braiding index value	1.77	1.69	- 4.8%
(*) total channel = active channel + islands			

335 **Table S4. 2003-2009 observed morphological processes**

Code	Feature class change	Area [m^2]	Morphological processes	Area [m^2]	Process percentage area [%]
T-B	Recent terrace → Gravel bar	36,800	Lateral erosion	56,600	2.5%
T-C	Recent terrace → Flowing and non-flowing channel	19,800			
T-V	Recent terrace → Active channel vegetation	200	Dissection	200	0.01%
I-B	Channel vegetation → Gravel bar	36,400	In-channel erosion	56,500	2.5%
V-C	Channel vegetation → Flowing and non-flowing channel	20,100			
B-B	Gravel bar → Gravel bar	1,091,700	Channel stability	1,839,000	80.2%
V-V	Active channel vegetation → Active channel vegetation	229,400			
C-C	Flowing and non-flowing channel → Flowing and non-flowing channel	148,900			
B-C	Gravel bar → Flowing and non-flowing channel	169,000			
C-B	Flowing and non-flowing channel → Gravel bar	200,000			
B-V	Gravel bar → Active channel vegetation	290,100	Vegetation establishment	340,100	14.8%
C-V	Flowing and non-flowing channel → Active channel vegetation	50,000			